

Comprehensive Compact Phenomenological Modeling of Integrated Metal-Oxide Memristors

Hussein Nili, Adrien F. Vincent, Mirko Preziosi, Mohammad R. Mahmoodi , Irina Kataeva, and Dmitri B. Strukov

Abstract—We present a comprehensive phenomenological model for the crossbar integrated metal-oxide continuous-state memristors. The model consists of static and dynamic equations, which are obtained by fitting a large amount of experimental data, collected on several hundred devices. Model describes the average devices' I-V characteristics as well as their spatial (device-to-device) and temporal variations. Both static and dynamic equations are explicit, computationally inexpensive, and suitable for SPICE modeling. The model's predictive power is validated using experimental data, while its utility by simulating image compression and image classification applications, two practical representative applications of mixed-signal memristor-based hardware.

Index Terms—Memristor, modeling, ReRAM, memristive crossbars, compact memristor model, phenomenological memristor model.

I. INTRODUCTION

THOUGH there has been significant progress in understanding the physics of operation for the metal-oxide ReRAM devices (also called memristors) [1]–[4], the development of accurate and comprehensive compact models has proven to be still very challenging. For the devices based on strongly-correlated materials, this is in part due to very rich transport and state-changing physics, because multiple mechanisms, e.g., switching due to ferroelectric domains, metal insulator transition, and drift of the defects, can be involved in the device operation [3], [4].

Indeed, most reported work (see, e.g., [4]–[8]) was based on physics models. This is very useful for verifying physical mechanisms, and as a guidance towards engineering of better devices. However, such models are generally inadequate for accurate and fast simulations, in part because of their focus on just certain aspects of the device operation, but also due to their implicit form, such as systems of coupled differential equations. The reported compact and SPICE models [9]–[13] are not sufficiently detailed (e.g., lacking device variations, temperature dependences) and/or accurate, largely because they are derived

based on simplified assumptions about resistive switching and electron transport mechanisms.

The need for accurate and comprehensive compact model of memristors is very acute now, given the recent advances in this technology and the increased focus on investigating memristors' potential for various applications. The main contribution of this paper is the development of such a model using a phenomenological approach. The proposed model is particularly useful for applications with ex-situ tuning such as neuromorphic inferences or PUFs [22], [23].

Three different metal-oxide memristors were considered—Pt/Al₂O₃/TiO_{2-x}/Ti/Pt with reactively sputtered Al₂O₃/TiO_{2-x} bilayer stack and Pt/Al₂O₃/TiO_{2-x}/Ti/Pt and Al/Al₂O₃/TiO_{2-x}/Ti/Al, in which Al₂O₃ was fabricated by atomic layer deposition. The devices of different types were integrated in the passive 20 × 20 crossbar arrays, with 200-nm lines separated by 400-nm gaps (Fig. 1).

Our most comprehensive model, described in Section 4, was developed for reactively sputtered Pt/Al₂O₃/TiO_{2-x}/Ti/Pt. The details of the fabrication technique, as well as extensive endurance and retention data, for such devices have been reported in Ref. [14]. The studied crossbar devices have uniform I-V characteristics with a narrow spread of set and reset voltages (Fig. 1(c)) - a critical requirement for the model development.

II. GENERAL MODELING APPROACH

We model the device behavior with two equations: $I = S(G_0, V, T)$ and $\Delta G_0 = D(G_0, V_p, t_p)$. The first, “static” equation describes the device current (I) as a function of the applied voltage (V), ambient temperature (T), and its memory state (represented by its low-voltage $G_0 \equiv I(0.1V)/0.1V$), at relatively small voltage biases (in our case, below 0.4 V) that do not modify the state, within the studied range of temperatures. The static model is specifically derived for small voltages and should not be used for extrapolation of currents at larger (write) voltages. The second, “dynamic” equation describes the change of the device's memory state as a function of its initial state after the application of a voltage pulse with some amplitude V_p and duration t_p . Such method of separating the static and dynamic behavior works well for most practical devices with strongly-nonlinear switching kinetics [8], [13].

These two equations are expressed as $S = S_m(G_0, V, T) + S_{d2d}(G_0, V, T) + S_N(V)$ and $D = D_m(G_0, V_p, t_p) + D_{d2d}(G_0, V_p, t_p)$, where S_m and D_m represent, respectively, the device's expected noise-free dc I-V curves and the expected conductance change ΔG , while S_{d2d} and D_{d2d} are their

Manuscript received October 22, 2019; revised January 3, 2020; accepted March 16, 2020. Date of publication April 27, 2020; date of current version May 29, 2020. This work was supported in part by Semiconductor Research Corporation funded JUMP CRISP Center, NSF/SRC E2CDA Grant 1740352, and in part by DENSO CORPORATION. The review of this article was arranged by associate editor Georgios Ch. Sirakoulis. (Corresponding author: Mohammad R. Mahmoodi.)

Hussein Nili, Adrien F. Vincent, Mirko Preziosi, Mohammad R. Mahmoodi, and Dmitri B. Strukov are with the University of California, Santa Barbara, CA, 93106 USA (e-mail: hnili@ucsb.edu; afvincent@ucsb.edu; mpreziosi@ucsb.edu; mrmahmoodi@ucsb.edu; strukov@ece.ucsb.edu).

Irina Kataeva is with the Research Laboratories, DENSO CORP., Komenoki-cho 470-0111, Japan (e-mail: IRINA_KATAEVA@denso.co.jp).

Digital Object Identifier 10.1109/TNANO.2020.2982128

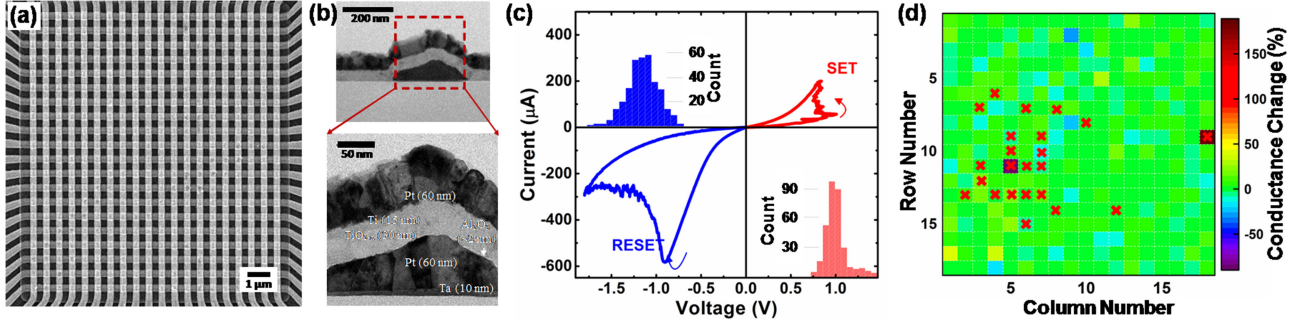


Fig. 1. Reproducible integrated metal-oxide memristors: (a) Top view SEM image of a 20×20 bilayer metal-oxide crossbar. (b) Cross-sectional TEM view of a single device in the crossbar array, with different metal and oxide layers identified. (c) Representative I - V characteristics and set-reset threshold statistics. (d) Conductance state retention (at 0.1 V) at the process of taking the I - V data for static modelling, at small non-disturbing biases (<0.4 V), and temperatures up to 100°C . Crosses denote the devices removed from fitting set, due to abnormal behavior.

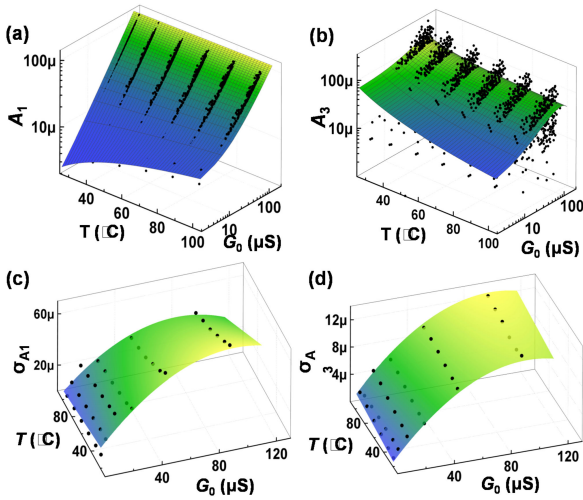


Fig. 2. Static model: (a, b) the data (dots) and fitting surfaces for the model parameters $A_1(G_0, T)$ and $A_3(G_0, T)$ and (c, d) their corresponding d2d variations. Specifically, in panels (c, d) the dots show standard deviations calculated for the A_1 and A_3 values in each bin, while the surfaces show their fitted functions.

normally-distributed stochastic d2d variations, and $S_N(V)$ is the temporal variations due to device's intrinsic noise.

III. MODELING RESULTS

To model the static behavior, we recorded dc I - V curves in the range -0.4 V to $+0.4$ V from 324 devices at 6 different temperatures: RT, 40, 55, 70, 85 and 100°C . All the curves have been then fitted with a cubic polynomial of the form $A_1(G_0, T)V + A_3(G_0, T)V^3$, mainly due to its simplicity. Subsequently, the A_1 and A_3 values are separately fitted to find the parameters μ_{A1} and μ_{A3} , (Fig. 2(a, b)) and σ_{A1} and σ_{A3} (Fig. 2(c, d)) that describe, respectively, the averages of A_1 and A_3 , and their effective standard deviations as functions of temperature and conductance. To make the model more representative, 22 outlier devices for which the parameter A_1 deviated by more than 50% from a quadratic surface fitting were excluded from the fitting set (Fig. 1(d)). The abnormal behavior in outlier devices easily manifest itself in A_1 since it is representative of linear conductance of the device. One possible

situation is the present of a defect in the device which causes low frequency current fluctuations (in a fixed bias, this would turn into fluctuations in conductance). A_3 on the other hand shows the nonlinearity of the device in relatively larger applied bias and is not the best parameter to detect the outliers.

Following this approach, the first two terms of the static equation can be written as $S_m = \mu_{A1} V + \mu_{A3} V^3$, and $S_{d2d} = N(0, 1) (\sigma_{A1} V + \sigma_{A3} V^3)$.

Crude estimates based on the reported low frequency noise [19]–[21] show that thermal noise will dominate at practical ($f > 100$ MHz) frequencies of operation. In this case variance of current fluctuations can be approximated as $k_B T f \times (I/V)$, where k_B is the Boltzmann constant, while $I = S_m + S_{d2d}$.

The same 324 devices were used for deriving the dynamic model. In this case, all devices were first randomly initialized to memory states within the $3.5 \mu\text{S}$ to $300 \mu\text{S}$ range. Each device was then subjected to 6,000 voltage pulses with random polarity and amplitude (from the ranges $[-0.8 \text{ V}, -1.5 \text{ V}]$ / $[0.8 \text{ V} \text{ to } 1.15 \text{ V}]$ for set / reset) and duration (from 100 ns to 100 ms), resulting in a total dataset size of ~ 2 million points that is covering uniformly the whole range of memory states. To avoid irreversible damage, the devices were not stressed beyond the studied range of conductances. Functions D_m and D_{d2d} were found separately for 8 ranges of memory states. For each range, D_m was found by fitting the data of all devices in each range to the empirically chosen exponential functions (Fig. 3). To obtain D_{d2d} , the coefficients of variation (CV) for conductance change were first calculated from the experimental data (Fig. 4), and then fitted with a polynomial function of V_p and $\log t_p$.

The functional forms and all fitting parameters for the baseline device technology are summarized in Table I.

IV. MODEL VERIFICATION

The accuracy of the static model was first validated using the R-squared measure, calculated for all the experimental I - V s and the ones defined by the S_m model (Fig. 5). Fig. 6 shows that the model can predict the average static behavior and d2d variations at different temperatures very well. The accuracy is worse for lower conductances, which is in part because of

TABLE I

SUMMARY OF THE MODEL AND ITS PARAMETERS FOR REACTIVELY SPUTTERED Pt/Al₂O₃/TiO_x/Ti/Pt CROSSBAR DEVICES. HERE $N[0, \sigma]$ IS A NORMALLY DISTRIBUTED RANDOM VARIABLE WITH ZERO MEAN AND STANDARD DEVIATION σ . NOTE THAT FOR EACH MEMRISTOR, RANDOM VARIABLE SHOULD BE SAMPLED ONCE TO MODEL DEVICE TO DEVICE VARIATION S_{d2d} AND REMAIN FIXED DURING SIMULATIONS. ON THE OTHER HAND, RANDOM VARIABLE SHOULD BE DRAWN FROM NORMAL DISTRIBUTION FOR EACH SAMPLE OF THE CURRENT TO GET ITS TEMPORAL FLUCTUATIONS S_N .

| Static Model | | | | | | | | | | | | | | | | | | | | |
|-----------------------------------|---|--|--------|-----------------------------|--|-------|-------|-----------------------------|-----------------------------|-----------------------------|-------------------------|-------|--|-----------------------------|---|-------|--|-----------------------------|-----------------------------|-----------------------------|
| $S_m(G_0, V, T)$ | $\mu_{A1}(G_0, T) \, V + \mu_{A3}(G_0, T) \, V^3$ | | | | | | | | | | | | | | | | | | | |
| $S_{d2d}(G_0, V, T)$ | $N[0,1] \times (\sigma_{A1}(G_0, T) \, V + \sigma_{A3}(G_0, T) V^3)$ | | | | | | | | | | | | | | | | | | | |
| $\mu_{A1}(G_0, T)$ | $a_0^{A1} + a_1^{A1} G_0 + a_2^{A1} T$ | | | | | | | | | | | | | | | | | | | |
| $\mu_{A3}(G_0, T)$ | $a_0^{A3} G_0 + a_1^{A3} G_0^2 + a_2^{A3} T^{-1.33}$ | | | | | | | | | | | | | | | | | | | |
| $\sigma_{A1}(G_0, T)$ | $p_0^{A1} + p_1^{A1} G_0 + p_2^{A1} T + p_3^{A1} G_0^2$ | | | | | | | | | | | | | | | | | | | |
| $\sigma_{A3}(G_0, T)$ | $p_0^{A3} + p_1^{A3} G_0 + p_2^{A3} T + p_3^{A3} G_0^2 + p_4^{A3} G_0 T$ | | | | | | | | | | | | | | | | | | | |
| $S_N(G_0, V, T)$ | $N[0, 4k_B T f(S_m(G_0, V, T) + S_{d2d}(G_0, V, T))/V]$ | | | | | | | | | | | | | | | | | | | |
| Dynamic Model | | | | | | | | | | | | | | | | | | | | |
| $D_m(G_0, V_p, t_p)$ | $c_0(\pm 1 - \tanh[c_1(\log t_p - c_2)])(\tanh[c_3 V_p - c_4] \pm 1)$, + for set, - for reset | | | | | | | | | | | | | | | | | | | |
| $D_{d2d}(G_0, V_p, t_p)$ | $N(0,1) \times D_m(G_0, V_p, t_p) \times (d_0 + d_1(\log t_p)^2 + d_2 V_p \log t_p + d_3 V_p^2 \log t_p + d_4 V_p^3)$ | | | | | | | | | | | | | | | | | | | |
| Model Parameters | | | | | | | | | | | | | | | | | | | | |
| <div><div></div><div></div></div> | a_0 | a_1 | | | a_2 | | | p_0 | | | p_1 | | p_2 | | p_3 | | p_4 | | | |
| A1 | -2.58e-6 [S] | 0.977 | | | 1.166e-7 [°C ⁻¹ S] | | | -1.07e-6 [S] | | | 0.25 | | 2.20e-8 [°C ⁻¹ S] | | -1300 [S ⁻¹] | | - | | | |
| A3 | 1.18 [V ⁻²] | 6596 [S ¹ V ⁻²] | | | 1.605e-3 [°C ^{-1.33} SV ⁻²] | | | 1.17e-5 [SV ⁻²] | | | 1.30 [V ⁻²] | | -1.0e-7 [°C ⁻¹ SV ⁻²] | | -6500 [S ¹ V ⁻²] | | -2.50e-3 [°C ⁻¹ V ⁻²] | | | |
| G_0 range (in μ S) | SET | | | | | | | | | | RESET | | | | | | | | | |
| | c_0 [S] | c_1 | c_2 | c_3 [V ⁻¹] | c_4 | d_0 | d_1 | d_2 [V ⁻¹] | d_3 [V ⁻²] | d_4 [V ⁻³] | c_0 [S] | c_1 | c_2 | c_3 [V ⁻¹] | c_4 | d_0 | d_1 | d_2 [V ⁻¹] | d_3 [V ⁻²] | d_4 [V ⁻³] |
| 3.16 – 5.62 | 1.55e-4 | -0.47 | -3.851 | 9.369 | 10.4 | -1.26 | -0.02 | 0.82 | -0.57 | 0.94 | -0.89e-4 | 0.89 | 8.96 | 6.2 | -10.90 | 0.04 | 2e-4 | 0.02 | 5e-3 | 0.03 |
| 5.62 – 10 | 1.55e-4 | -0.47 | -3.769 | 7.512 | 8.419 | -1.22 | -0.02 | 0.84 | -0.57 | 0.81 | -0.89e-4 | 0.51 | 6.88 | 6.2 | -8.61 | -5e-3 | -4e-4 | -2e-3 | -0.01 | 0.02 |
| 10 – 17.8 | 1.55e-4 | -0.47 | -3.729 | 6.801 | 7.582 | -1.03 | -0.02 | 0.72 | -0.47 | 0.63 | -0.89e-4 | 0.34 | 4.93 | 6.2 | -8.14 | -0.07 | -3e-3 | -0.07 | -0.05 | -0.02 |
| 17.8 – 31.6 | 1.55e-4 | -0.47 | -3.517 | 6.180 | 6.851 | -0.78 | -0.01 | 0.53 | -0.33 | 0.45 | -0.89e-4 | 0.25 | 3.63 | 6.2 | -7.77 | -0.11 | -4e-3 | -0.11 | -0.09 | -0.03 |
| 31.6 – 56.2 | 1.55e-4 | -0.47 | -3.426 | 5.946 | 6.558 | -0.37 | 5e-3 | 0.15 | -0.01 | 0.11 | -0.89e-4 | 0.23 | 2.91 | 6.2 | -7.42 | -0.15 | -6e-3 | -0.17 | -0.13 | -0.06 |
| 56.2 – 100 | 1.55e-4 | -0.47 | -3.373 | 5.005 | 5.792 | 0.14 | 0.01 | -0.29 | 0.31 | -0.21 | -0.89e-4 | 0.21 | 2.33 | 6.2 | -7.30 | -0.12 | -5e-3 | -0.16 | -0.13 | -0.06 |
| 100 – 178 | 1.55e-4 | -0.47 | -3.422 | 4.936 | 5.840 | 0.34 | 0.01 | -0.41 | 0.37 | -0.29 | -0.89e-4 | 0.22 | 1.93 | 6.2 | -7.10 | -0.04 | -2e-3 | -0.10 | -0.11 | -0.04 |
| 178 – 316 | 1.55e-4 | -0.47 | -3.572 | 4.864 | 5.785 | 0.26 | 0.01 | -0.29 | 0.25 | -0.20 | -0.89e-4 | 0.28 | 1.68 | 6.2 | -7.00 | 0.10 | 3e-3 | 0.02 | -0.05 | -4e-3 |

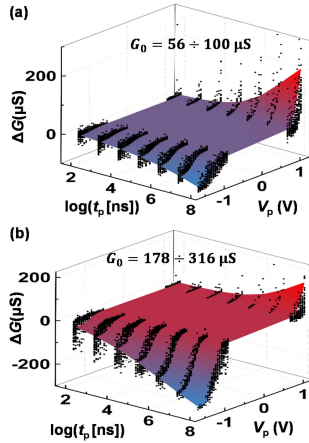


Fig. 3. Dynamic model: The measured absolute change in conductance at 0.1 V as a function of the amplitude (V_p) and duration (t_p) of the applied voltage pulse for two state ranges (out of 8 total used). On each panel, dots show the experimental data for the devices with the initial memory states in that range. The surfaces show the corresponding fitted functions.

fewer experimental data in this region. Additionally, this is due to non-negligible leakage currents in the crossbar circuits, which makes accurate measurements of low currents via selected device challenging.

Finally, the accuracy of the dynamic model was partially verified by contrasting the statistics of the experimentally observed

conductance changes under different applied voltage pulses, and the ones predicted by the models (Fig. 7(a, b)). Fig. 7(c, d) also shows the simulated evolution of conductance (at 0.1 V) for 5 devices, demonstrating the role of pulse stress conditions and device-to-device variations in the dynamic behavior.

V. EXAMPLES OF MODEL APPLICATIONS

The developed model is useful for guiding the design automation for analog and mixed-signal computing circuits based on integrated analog-state memristors. To provide a meaningful example and further verify the model, we have studied two such prospective applications—image compression/decompression using discrete cosine transform algorithm and ex-situ trained image classifier. For both applications, the most common operation is vector-by-matrix multiplication (VMM) operation, which can be efficiently implemented with mixed-signal memristor-based crossbar circuits [14].

For the first study, we used similar approach discussed in Ref. [15], with image compression and restoration implemented using 8×8 discrete cosine transform kernels (Fig. 8). The algorithm performance was compared for three cases: an ideal (full precision) software model (a resistor with 64-bit computational accuracy); a software emulation of the memristor-based hardware in which VMM was modelled using the described device model; and demonstration based on experimental VMM

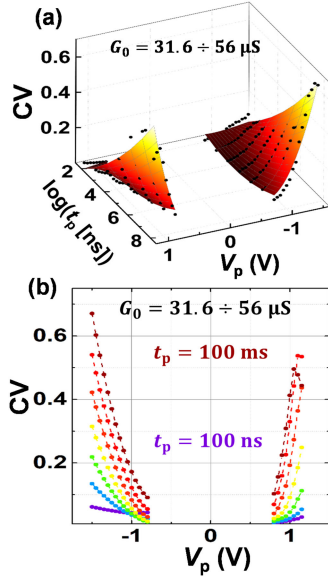


Fig. 4. Dynamic model for device-to-device variations: (a) 3D and (b) 2D graphs of the coefficients of variation and their polynomial fits for a representative conductance range.

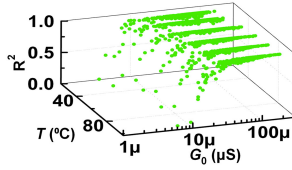


Fig. 5. The goodness-of-fitting (R^2 measure) obtained with S_m function applied to all experimental I - V curves.

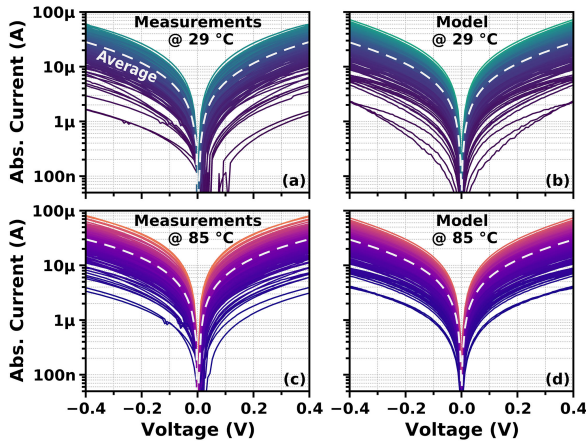


Fig. 6. Comparison between the experimental I - V curves measured from 200 random devices and the simulated I - V curves based on $I = S(G_0, V, T)$, using a similar set of initial conductances at 0.1 V at 29° and 85° C.

results measured on crossbar integrated memristors. (For the second case, only I - V non-idealities were considered, while other imperfections, such as finite wire resistance, nonlinearity of peripheral circuits, were neglected, which is justified for such small kernels.) Fig. 9(e) shows that the simulated results (using Cadence Virtuoso framework) for pixel intensities of the

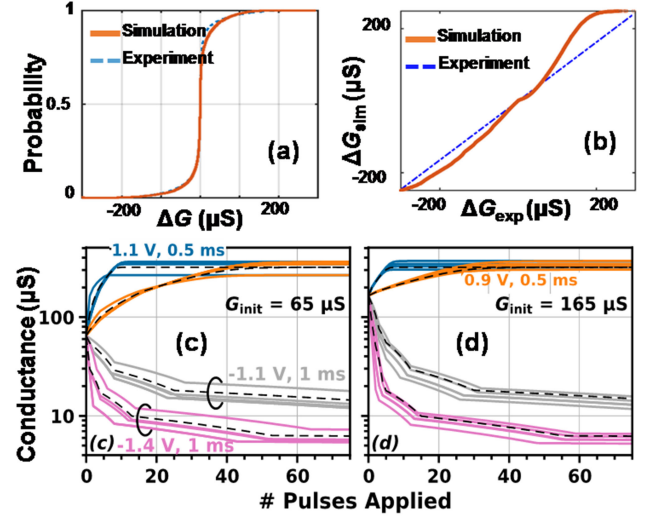


Fig. 7. Dynamic model verification: (a) CDF of all experimental ΔG values and the corresponding simulated values. (b) Q-Q plot of simulated vs. experimental values. (c, d) Simulated conductance evolution of 5 devices, combining $D(G_0, V_p, t_p)$ and $S(G_0, V, T)$. For each device, 2 different initial conductance values and 4 different types of pulses have been used, to generate a total of 8 combinations.

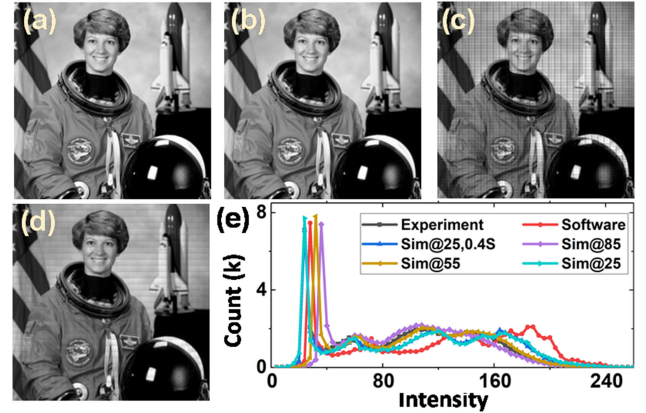


Fig. 8. Compressing and decompressing an image using DCT algorithm: (a) an original and (b–d) reconstructed images, obtained by (b) device-oblivious full precision simulations, (c) experimentally measured data, and (d) using the proposed model. (e) The histograms of the pixel intensities for reconstructed images. The standard deviation for the pixel intensity differences between (c) and (d) images, normalized to the maximum brightness, is less than 5%.

reconstructed image follow closely the experimentally measured data. Moreover, the simulation results based on the device model are in better correspondence, as compared to the ideal software model, with experiment.

Additionally, the model was applied to simulate the impact of temperature variations and device imperfections on the functional performance of ex-situ trained medium-scale image classifiers (Fig. 9). Four medium-scale neural network models are considered: a multilayer perceptron with one hidden layer of 300 neurons, a 4-layer convolutional neural network (CNN) trained on MNIST data set, a 7-layer CNN trained on GTSRB data set, and a 5-layer CNN trained on CIFAR-10 data set. The latter was implemented with two different activation functions, ReLU and tanh, to investigate the impact of the activation function choice

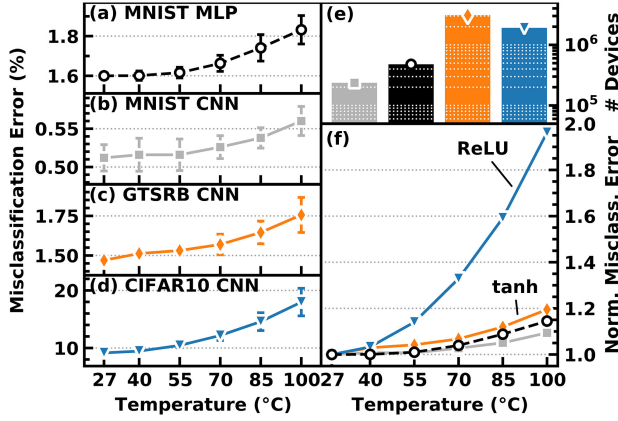


Fig. 9. Application of the model for simulation of ex-situ trained mixed-signal image classifiers for (a,b) MNIST, (c) GTSRB, and (d) CIFAR10 benchmarks. The neural network parameter and training procedure is similar to those used in [12], [13]. (e) The number of memristors utilized in each simulated network. (f) The misclassification error for considered cases, normalized by its value at 27 °C.

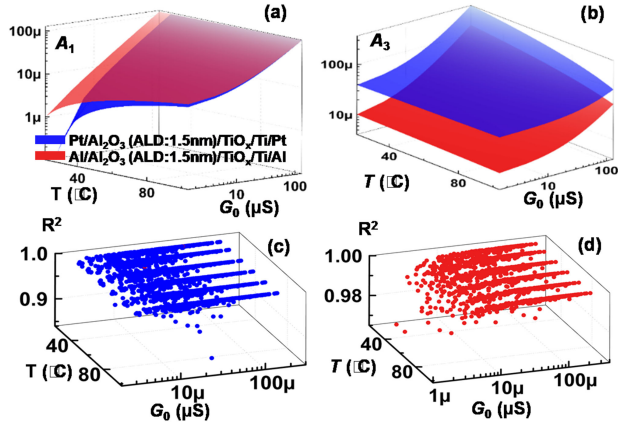


Fig. 10. The static model results obtained similarly to those of Figs. 2 and 5 for two other types of studied devices (with different deposition approach and electrode material).

on recognition performance. The training was simulated by first finding weights (w) for the hardware-independent full-precision (64-bit) software implementation of the network. The weights were then mapped to the corresponding differential memristors' conductances at 0.1 V and 27 °C.

Interestingly, the modelling results predicts rather negligible dependence of classifier performance on ambient temperature for MNIST datasets, which has been observed experimentally for mixed-signal implementations [18].

VI. DISCUSSION AND SUMMARY

Although the model has been developed for a particular (though representative) fabrication technology, this approach to memristor modelling is quite general and can be applied to other types of such devices. For example, Fig. 10 shows preliminary results for two other considered types of devices, for which similar polynomial functions, but with different fitting parameters, were successfully used to model the static behavior.

While we showed the results for three devices, it is a future work to apply the modeling approach on other stacks. The model provides useful insights on nonlinearity, variations, and temperature dependency which aids process designers tune their recipes. In addition, although the (main) result is provided based on a certain device stack, it can be still very useful in many studies, setting the modeling methodology aside. Indeed, we believe that there are many researchers interested in using a model which fits very well to actual measurements of real devices, regardless of its type. Citing the context of physically unclonable functions as an example, we think that using a generic model has no use. This stems from the fact that the circuit response (cryptographic keys) are heavily correlated with the process-induced variations and it is imperative to use simulation models which capture them properly.

It is worth noting that in the current form, the model is not predictive, since it's fitting parameters cannot be tied, at least directly, to the specific properties of the utilized materials and device geometry. Its primary purpose is to enable accurate simulations of large scale memristor-based systems rather than guide the development of better devices. However, the choice of the fitting functions may be further guided by plausible physical mechanisms. In fact, the polynomial function used in the static equation fitting had been already motivated by a plausible conduction model, with the linear part representing the Ohmic conductance of vacancy-doped filaments, while the nonlinear one approximating the bulk trap-limited conduction of the insulating parts of the metal-oxide layer and/or the charge-carrier injection at the interfaces.

The static model, as expected, is based on quasi-DC measurements performed at various (low, <0.4 V) voltages. This would decouple the impact of parasitics, which are important at high frequency applications from the present work. Having said that, modeling the parasitics (e.g., wire conductance and capacitance) is fairly straightforward, if needed. The model can be used with any types of stimulus very accurately at low frequencies. For high frequencies, the parasitics (which should be in the order of ~ 10 aF and $\sim 1\Omega$ per device) must be included in the simulation setup.

The dynamic model is developed based on square-pulse stimulus, which is used in most analog applications of resistive memories. Whether it is a neural network, matrix multiplication, hardware security, etc., memristive devices are often tuned by write-verify algorithm, which uses pulse train waveform for altering the conductances. Therefore, we have simplified the modeling and focused on pulse waveforms."

In summary, our paper presents a comprehensive compact model for metal-oxide memristors, which is developed via empirical fitting of the measured data. The model includes static and dynamic characteristics, their device-to-device variations, temperature effects, and noise. The functionality of the model has been demonstrated using two case studies of practical memristive networks.

APPENDIX

The static model of the device in Verilog-A is available from <https://www.ece.ucsb.edu/~strukov/model> to download.

REFERENCES

- [1] P. H.-S. Wong *et al.*, “Metal-oxide RRAM,” *Proc. IEEE*, vol. 100, no. 6, pp. 1951–1970, Jun. 2012.
- [2] J. J. Yang, D. B. Strukov, and D. R. Stewart, “Memristive devices for computing,” *Nature Nanotechnol.*, vol. 8, pp. 13–24, 2013.
- [3] D. S. Jeong *et al.*, “Emerging memories: Resistive switching mechanisms and current status,” *Rep. Prog. Phys.*, vol. 75, 2012, Art. no. 076502.
- [4] D. Ielmini, “Resistive switching memories based on metal oxides: mechanisms, reliability and scaling,” *Semicond. Sci. Technol.*, vol. 31, 2016, Art. no. 063002.
- [5] M. Pickett *et al.*, “Switching dynamics in a titanium dioxide memristive device,” *J. Appl. Phys.*, vol. 106, 2009, Art. no. 074508.
- [6] S. Larentis, F. Nardi, S. Balatti, D. C. Gilmer, and D. Ielmini, “Resistive switching by voltage-driven ion migration in bipolar RRAM—Part II: Modelling,” *IEEE Trans. Electron Devices*, vol. 59, no. 9, pp. 2468–2475, Sep. 2012.
- [7] X. Guan, S. Yu, and H.-P. Wong, “On the switching parameter variation of metal-oxide RRAM-Part I: Physical modelling and simulation methodology,” *IEEE Trans. Electron Devices*, vol. 59, no. 4, pp. 172–182, Apr. 2012.
- [8] S. Kim *et al.*, “Comprehensive physical model of dynamic resistive switching in an oxide memristor,” *ACS Nano*, vol. 8, pp. 2369–2376, 2014.
- [9] X. Guan, S. Yu, and H.-P. Wong, “A SPICE compact model of metal oxide resistive switching memory with variations,” *IEEE Electron Device Lett.*, vol. 33, no. 10, pp. 1405–1407, Oct. 2012.
- [10] J.P. Strachan *et al.*, “State dynamics and modeling of tantalum oxide memristors,” *IEEE Trans. Electron Devices*, vol. 60, no. 7, pp. 2194–2202, Jul. 2013.
- [11] F. G.-Redondo, R. P. Gowers, A. C.-Yepes, M. L.-Vallejo, and L. Jiang, “SPICE compact modelling of bipolar/ unipolar memristor switching governed by electrical thresholds,” *IEEE Trans. Circuit Syst. –I*, vol. 63, no. 8, pp. 1255–1264, Aug. 2016.
- [12] F. Merrikh Bayat *et al.*, “Phenomenological modeling of memristive devices,” *Appl. Phys. A*, vol. 118, pp. 770–786, 2015.
- [13] S. Kvatinsky, E.G. Friedman, A. Kolodny, and U. C. Weiser, “TEAM: Threshold adaptive memristor model,” *IEEE Trans. Circuit Syst. –I*, vol. 60, no. 1, pp. 211–221, Jan. 2013.
- [14] F. Merrikh Bayat *et al.*, “Implementation of multilayer perceptron network with highly uniform passive memristive crossbar circuits,” *Nat. Commun.*, vol. 9, 2018, Art. no. 2331.
- [15] C. Li *et al.*, “Analogue signal and image processing with large memristor crossbars,” *Nature Electron.*, vol. 1, pp. 52–59, 2018.
- [16] I. Kataeva, F. Merrikh-Bayat, E. Zamanidoost, and D. Strukov, “Efficient training algorithms for neural networks based on memristive crossbar circuits,” in *Proc. Int. Joint Conf. Neural Netw.*, Killarney, Ireland, Jul. 2015, pp. 1–8.
- [17] M. Prezioso *et al.*, “Modeling and implementation of firing-rate neuromorphic-network classifiers with bilayer Pt/Al₂O₃/TiO_{2-x}/Pt memristors,” in *Proc. IEEE Int. Electron Devices Meeting*, Washington, DC, USA, Dec. 2015, pp. 17.4.1–17.4.4.
- [18] X. Guo *et al.*, “Fast, energy-efficient, robust, and reproducible mixed-signal neuromorphic classifier based on embedded NOR flash memory technology,” in *Proc. IEEE Int. Electron Devices Meeting*, San Francisco, CA, USA, Dec. 2017, pp. 6.5.1–6.5.4.
- [19] Z. Fang *et al.*, “Low-frequency noise in oxide-based (TiN/HfO_x/Pt) resistive random access memory cells,” *IEEE Trans. Electron Devices*, vol. 59, no. 3, pp. 850–853, Mar. 2012.
- [20] F. Puglisi *et al.*, “Random telegraph noise in resistive random access memories: Compact modeling and advanced circuit design,” *IEEE Trans. Electron Devices*, vol. 65, no. 7, pp. 2964–2972, Jul. 2018.
- [21] S. Ambrogio *et al.*, “Impact of low-frequency noise on read distributions of resistive switching memory (RRAM),” in *Proc. IEEE Int. Electron Devices Meeting*, San Francisco, CA, USA, Dec. 2014.
- [22] H. Nili *et al.*, “Hardware-intrinsic security primitives enabled by analogue state and nonlinear conductance variations in integrated memristors,” *Nature Electron.*, vol. 1, 2018, Art. no. 197.
- [23] M. Prezioso, *et al.*, “Spike-timing-dependent plasticity learning of coincidence detection with passively integrated memristive circuits,” *Nature Commun.*, vol. 9, 2018, Art. no. 5311.